



Article

Retrieval of Daily Mean VIIRS SST Products in China Seas

Qianmei Li ^{1,2} , Qingyou He ^{1,3,4} and Chuqun Chen ^{1,2,3,*}

¹ State Key Laboratory of Tropical Oceanography, South China Sea Institute of Oceanology, Chinese Academy of Sciences, Guangzhou 510301, China; qianmeili@scsio.ac.cn (Q.L.); qyhe@scsio.ac.cn (Q.H.)

² University of Chinese Academy of Sciences, Beijing 100049, China

³ Southern Marine Science and Engineering Guangdong Laboratory (Guangzhou), Guangzhou 511458, China

⁴ Guangdong Key Laboratory of Ocean Remote Sensing, South China Sea Institute of Oceanology, Chinese Academy of Sciences, Guangzhou 510301, China

* Correspondence: cqchen@scsio.ac.cn

Abstract: Sea surface temperature (SST) is one of the most important factors in regulating air-sea heat flux and, thus, climate change. Most of current global daily SST products are derived from one or two transient measurements of polar-orbiting satellites, which are not the same to daily mean SST values. In this study, high-temporal-resolution SST measurements (32–40 snapshots per day) from a geostationary satellite, FengYun-4A (FY-4A), are used to analyze the diurnal variation of SST in China seas. The results present a sinusoidal pattern of the diurnal variability in SST, with the maximum value at 13:00–15:00 CST and the minimum at 06:00–08:00 CST. Based on the diurnal variation of SST, a retrieval method for daily mean SST products from polar-orbiting satellites is established and applied to 7716 visible infrared imaging radiometer (VIIRS) data in China seas. The results suggest that it is feasible and practical for the retrieval of daily mean SST with an average RMSE of 0.133 °C. This retrieval method can also be utilized to other polar-orbiting satellites and obtain more daily mean satellite SST products, which will contribute to more accurate estimation and prediction between atmosphere and ocean in the future.

Keywords: sea surface temperature; VIIRS; FY-4A; diurnal variation; daily mean SST



Citation: Li, Q.; He, Q.; Chen, C. Retrieval of Daily Mean VIIRS SST Products in China Seas. *Remote Sens.* **2021**, *13*, 5158. <https://doi.org/10.3390/rs13245158>

Academic Editors: Mitchell D. Goldberg, Alexander Ignatov, Satya Kalluri, Paul M. DiGiacomo and Changyong Cao

Received: 3 November 2021
Accepted: 15 December 2021
Published: 19 December 2021

Publisher's Note: MDPI stays neutral with regard to jurisdictional claims in published maps and institutional affiliations.



Copyright: © 2021 by the authors. Licensee MDPI, Basel, Switzerland. This article is an open access article distributed under the terms and conditions of the Creative Commons Attribution (CC BY) license (<https://creativecommons.org/licenses/by/4.0/>).

1. Introduction

Sea surface temperature (SST) is an important parameter in marine hydrography, playing essential roles in regulating physical and biogeochemical environments in the global ocean [1]. As a key variable of marine ecosystems, SST affects the growth rate of phytoplankton community [2] and indicates the potential favorable area for fish gathering [3], providing theoretical basis and reference for fishery forecast [4]. As a crucial physical quantity in the global air-sea interaction processes, SST controls the heat transmission in the oceanic boundary layer and couples the ocean-atmosphere system and is frequently applied in the boundary condition of atmospheric models [5]. Initially, SST data were obtained from in situ measurements such as ships, buoys and ocean stations, which are difficult to carry out and the derived measurements have poor spatial-temporal continuity. With the development of remote sensing technology, satellite-retrieved SST products are widely used with wide coverage and strong real-time performance. In addition, they are mainly utilized in the studies of water mass properties [6], ocean circulation [7], tropical cyclone [8], weather prediction [9] and ocean numerical simulation [10,11]. In these research areas, the quality of satellite SST products has becoming a prerequisite influencing the scientific findings. In another word, high-quality SST products are essential for oceanographic research.

Numerous efforts have been paid to improve the accuracy of satellites SST measurements, including advancement of instruments, improvement of in-orbit calibration, upgrade of inversion algorithms and optimization of quality control procedures [12–17].

However, an inevitable fact is that most of global daily SST products were based on instantaneous observations from polar-orbiting satellites with a sampling rate of 1–2 times a day, which cannot represent the real daily mean SST. This is because that SST vary dramatically in a day due to the diurnal variability of solar radiation [18].

Stramma et al. [19] reported that the maximum diurnal difference of SST between day and night reached 3.5 °C in the Sargasso Sea. Based on data of Advanced Very High Resolution Radiometer (AVHRR) off northern California, model analysis revealed that that the diurnal variation of SST could be greater than 6.6 °C under special conditions [20]. According to Gentemann et al. [21], in the extratropical ocean, the diurnal variability in SST reached up to 5–7 °C under low wind speed and high insolation, which was equivalent to the magnitude of SST seasonal variability. Previous studies showed that diurnal variability in SST is considered to be responsible for the large deviation (10 W/m²) of air-sea latent and sensible heat flux in the numerical simulation [22], the increase in ENSO amplitude (by 15%) in air-sea coupled model [23] and the deviation (4.5 W/m²) of the annual mean air-sea heat flux around the world [24]. Overall, the instantaneous SST at a time of day is not the same to the daily mean SST.

Some studies, such as creation of early warning system for severe weather events [25], estimation of daily mean air-sea flux [1], model of regional atmosphere-ocean coupling [26] and the recruitment index and larval survival index of *Pandalus borealis* [27], may require daily mean SST as input parameters. However, there are no available public data of daily mean SST by high accuracy satellite sensors. Meanwhile, weekly and monthly SST products are calculated from instantaneous daily SST products [28] and they are not the actual weekly and monthly mean SST products. Therefore, we propose a method to retrieve daily mean SST products from open satellite SST products.

The Visible Infrared Imaging Radiometer (VIIRS) is considered to be an extension and improvement of Moderate Resolution Imaging Spectroradiometer (MODIS) and AVHRR, providing long-term measurements for climate research, weather forecasting and disaster relief [29]. It captures diurnal cycle of SST at only two points, for consistency with the Advanced Geosynchronous Radiation Imager (AGRI) which has the capability to resolve the full diurnal cycle. AGRI on the recent launched China's new geostationary satellite FY-4A has sampling interval of 15 min and a satellite zenith of 0–59° (Figure 1), enabling continuous observation under 24 h. Here, the high-temporal resolution SST products of AGRI (Figure 1) from June 2018 to May 2019 are applied to investigation of the diurnal variability in SST in the China seas (0–45°N, 103–133°E). The derived diurnal change rules of SST are further used to establish a retrieval for 7716 instantaneous SST products of VIIRS in China seas. Finally, we get high-accuracy daily mean VIIRS SST products, which are crucial for marine climate monitoring and numerical simulation.

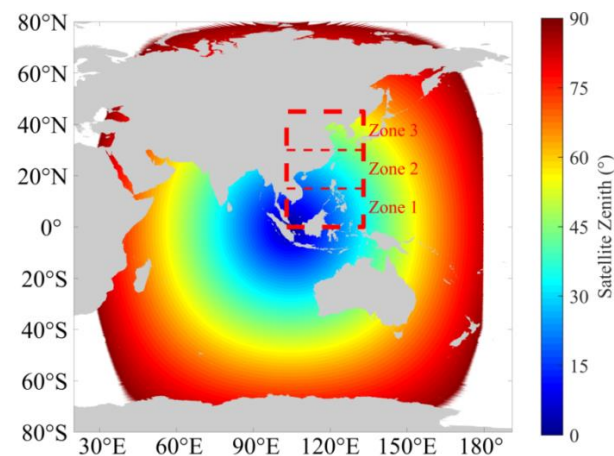


Figure 1. Satellite zenith distribution of FY-4A/AGRI scanning range to the earth (Gray filled area is land mask. Bold red dashed frame represents sea area studied in this paper). Zone 1 to Zone 3 are used in the discussion of diurnal variation of SST in different zones in the latter part of this paper.

2. Materials and Methods

2.1. S-NPP/VIIRS SST

The Suomi National Polar-orbiting Partnership (S-NPP) Satellite placed in orbit 28 October 2011 is a part of Joint Polar Satellite System (JPSS) [30]. The pass times of S-NPP are approximately 1:30 a.m. (descending path) and 1:30 p.m. local time (ascending path). VIIRS on S-NPP satellite has a nominal altitude of 824 km with swath width of 3600 km and provides 22 bands range from 0.4 μm to 12.5 μm with a spatial resolution of 375–750 m [31]. On-orbit calibration of the VIIRS channels is performed with a spatial perspective and a blackbody radiation source, which could diminish orbital temperature changes driven by external factors [32]. The processing for cloud detection and SST retrieval from VIIRS images is completely dependent on five bands with central wavelength of 0.67 μm (M5), 0.87 μm (M7), 3.7 μm (M12), 10.7 μm (M15) and 12.0 μm (M16) [33]. In addition, it is done by dividing a granule into 10×6 pixels-windows termed “target array” and retrieving from cloud-screened 2×2 pixel unit arrays [34]. In addition, the operational VIIRS SST products used in this article are retrieved from the improved algorithm of the Naval Oceanographic Office (NAVO) based on the nonlinear algorithm (NLSST) of MODIS and AVHRR. VIIRS measurements are regressed to a nominal depth of 1 m [33]. The level-2 products of VIIRS NAVO SST are integrated into the Group for High-Resolution SST (GHRSSST) and added a 0–5 quality flag in accordance with the GHRSSST data processing specification. These data products are publicly obtained from https://www.ncei.noaa.gov/data/oceans/ghrsst/L2P/VIIRS_NPP/NAVO/ (accessed on 28 October 2019).

2.2. FY-4A/AGRI SST

FY-4A is a new generation of China’s geostationary meteorological satellite, which was successfully launched in December 2016 and located at 104.7°E. The observation instruments, data collection system and processing algorithm carried by FY-4A satellite are independently developed by China and most of technical indicators are at the cutting-edge level of Chinese industry [35]. The FY-4 satellite, together with the Geostationary Operational Environmental Satellite (GOES-R), Himawari satellite and European Meteorological Satellite (EUMETSAT), forms an international constellation of geostationary satellites, providing global observations and predictions of environment. The AGRI which is one of the main payloads of FY-4A uses the self-developed two-dimensional scanning technology and image navigation registration technology to realize imaging of the whole disk of the earth, significantly improving the observation efficiency and image registration accuracy. AGRI contains 14 spectral bands from visible to infrared at spatial resolutions of 0.5–4.0 km. In the meantime, it obtains a full disk image at 15 min interval, with on-board radiometric calibration accuracy and sensitivity of 0.5 K and 0.2 K [36]. The spatial coverage of AGRI images is capacious, with longitudinal and latitudinal limits of about $\pm 80^\circ$ and satellite zenith angle of exceed 70° . The main task is to improve the quantitative monitoring capability of various physical variables in the earth surface and atmosphere by means of continuous observation at the same location with full-time and full-weather. Level-2 SST products are obtained after radiation calibration, cloud detection, inversion calculation and quality control of level 1 data. Among them, cloud detection is carried out by the different spectral and spatial characteristics of the 6 bands (center at 0.65 μm , 1.61 μm , 3.75 μm , 7.1 μm , 10.8 μm and 12.0 μm) in the case of cloudy and clear sky [37]. The SST retrieval is calculated based on the operational inversion algorithm proposed by Walton [38] and the quality flag of 0–3 is added, which can be publicly achieved via <http://satellite.nsmc.org.cn/PortalSite/> (accessed on 29 November 2019).

2.3. In Situ SST

The in situ SST data used for validation of satellite data are from the in situ SST Quality Monitor system (iQuam) developed by NOAA. Data in the system are collected from various platforms, including ship, drifting buoy, coastal moored buoy, tropical moored

buoy, Argo float, high resolution drifter, integrated marine observing system and coral reef watch buoy, carried out by different countries and institutions. Due to the differences in the characteristics and accuracy of various measuring instruments, as well as the deviation introduced by instrument aging, failure and misoperation, the iQuam system carries out strict quality control on the data, aiming to provide unified high-accuracy in-situ SST products for scientific research. In addition to the basic screening techniques (deduplication removal, geolocation check, platform track check and SST spike check), the quality control algorithm also contains more complex reference check and cross-platform check [39], which utilize the Bayesian-based approach by Lorenc and Hammon [40]. As a component data of the GHRSSST system, iQuam data provides a great help for data fusion and validation of various SST satellite products. These data products are publicly acquired from <https://www.star.nesdis.noaa.gov/socd/sst/iquam/> (accessed on 18 October 2019).

2.4. Quality Control

Since the analysis of SST diurnal variation characteristics requires high-quality data, it is essential to eliminate outliers through quality control for data reliability. Based on time and space consistency, a quality control procedure of SST datasets is established in this paper. Firstly, the Global Self-consistent, Hierarchical, High-resolution Geography (GSHHG) database provided by NOAA is utilized to identify inland water pixels. Secondly, SST values are usually uniformly distributed or gradually changing; hence, the root mean square error of SST in the data grid of $n \times n$ ($2 \leq n \leq 5$) is relatively small. A sliding data detection window of 3×3 is established for statistical calculation of each pixel. If root mean square error of the 9 pixels in the detection window is greater than 1°C , the central pixel will fall into disuse. Then, the 24 h of a day in Chinese standard time (CST, times presented in this paper are CST) are divided into 12 groups and the images of each 2 h are as one group in chronological order. If 12 groups of a same pixel all contain valid values, the pixel will be recorded as valid, otherwise it will be eliminated. Then, a quartile robust statistics technique is used to estimate the median and robust standard deviation (RSD) and the results are less affected by outliers than the traditional estimators [41]. The data of the same pixel at different moments in a day are set as a group and detected one by one where the threshold is $\text{median} \pm 3 \times \text{RSD}$, where RSD is defined as $(3\text{rd quartile} - 1\text{st quartile})/1.3848$ [42]. After the previous quality inspection steps, the remaining pixels are reliable clear-sky data of ocean.

2.5. Matchups and Validation

Before verifying the accuracy of remote sensing inversion data, it is necessary to match up the satellite data to in situ observations in time and space domain, which can limit the possible influence of SST diurnal variation. For each in situ measurement, the near-simultaneous (within ± 30 min) satellite products are selected. The spatial matching is based on the nearest neighbor principle, namely, that the arithmetic average value of in-situ data contained in each remote sensing pixel cell will be calculated.

In this paper, the China seas ($0\text{--}45^\circ\text{N}$, $103\text{--}133^\circ\text{E}$) are taken as an example (Figure 2) and a total of 6806 matchups between FY-4A/AGRI SST and iQuam SST are obtained between June 2018 and May 2019. In comparison, the root mean square error (RMSE) of these matchups is 0.6961°C and the correlation coefficient is 0.9714, indicating that the AGRI SST data are highly accurate and strongly correlated with the iQuam SST data.

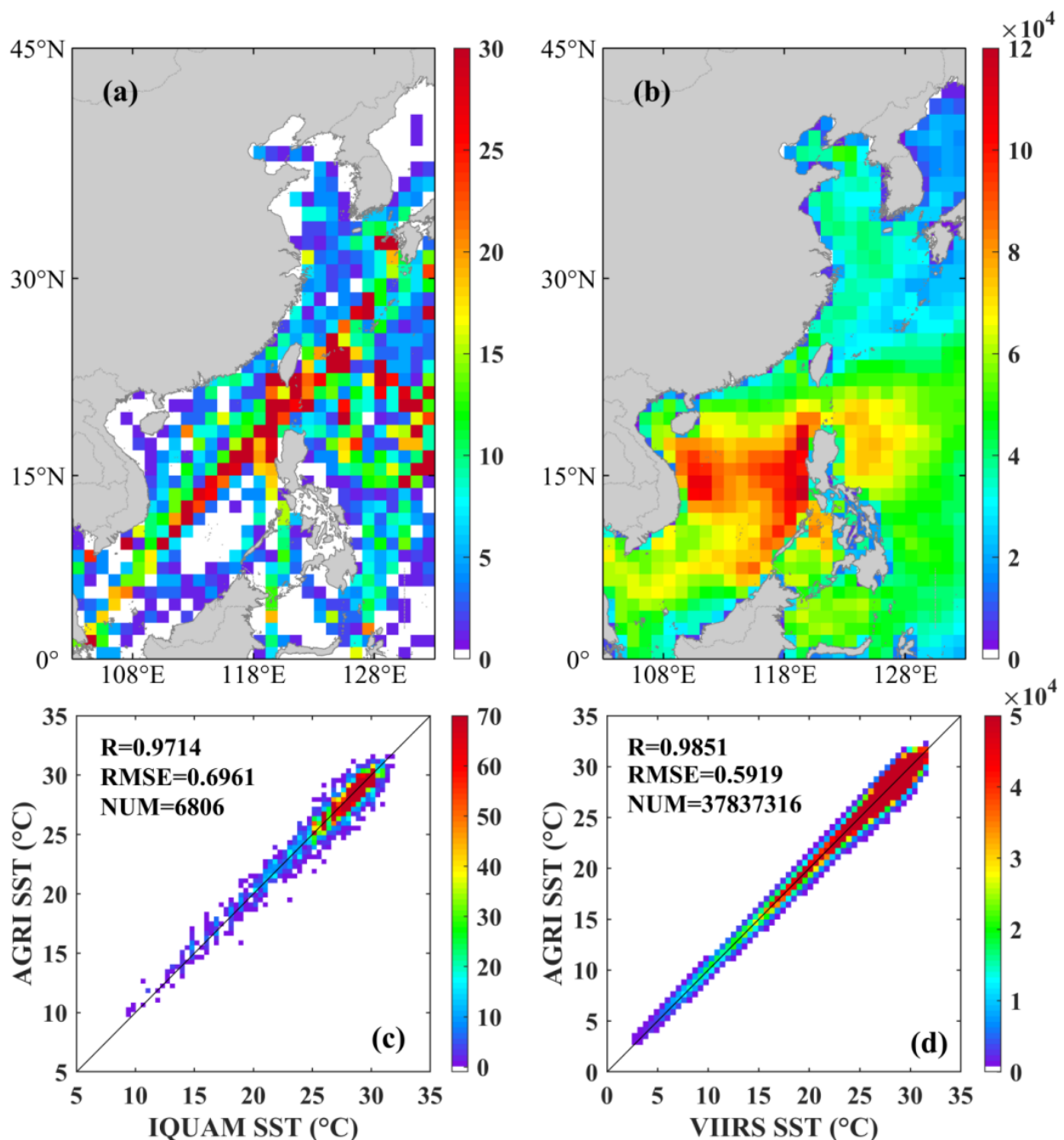


Figure 2. Distribution of FY-4A/AGRI matchups with (a) in-situ measurements and (b) S-NPP/VIIRS respectively, during June 2018 to May 2019 in China seas. The colors are the number of matchups in $1^\circ \times 1^\circ$ resolution. Frequency diagrams (c,d) plotting SST comparison of matchups in figures (a,b), respectively. The colors denote the total number of SST values in each $0.5^\circ\text{C} \times 0.5^\circ\text{C}$ box.

At the same time, we match up the S-NPP/VIIRS SST data to the FY-4A/AGRI SST data for the purpose of retrieval of daily mean SST. For temporal resolution, the sampling rate of VIIRS (only 1–2 times per day) is less than that of AGRI (32–40 times per day). In addition, its equator-crossing time is 13:30 CST; hence, AGRI selects 13:45 CST data which is with no more than 30 min interval. In terms of spatial resolution, AGRI (4 km) is lower than VIIRS (0.75 km) and the movement detection window is established based on pixel size of AGRI. The values of VIIRS pixels falling into a single window are averaged to obtain the matching data corresponding to AGRI. There are 37,837,316 SST matchups of AGRI and VIIRS, with RMSE of 0.5919 °C and correlation coefficient of 0.9851. The results

demonstrate that AGRI SST has a strong correlation with VIIRS SST and it is feasible to obtain the daily mean VIIRS SST by scaling the daytime VIIRS SST with factors derived from AGRI data.

3. Results

3.1. Case Analysis

Previous researches have demonstrated that there are a large number of diurnal warming events in China seas [41,43] and the temporal evolution of the China seas on 9 February 2019 is analyzed for a direct insight of SST diurnal variation (Figure 3). Because of large temperature difference between low and high latitudes, the characteristics of SST diurnal variation are difficult to be discerned. Thus, we calculate the SST variation (SST_{dv}) at different hours relative to the daily mean temperature in the day. Figure 3 shows the spatial distribution of SST_{dv} in the study area, with intervals of 4 h. The results show that the lowest SST in a day appears at 6:00 CST and it is $0.40\text{ }^{\circ}\text{C}$ lower than the mean value of the day. Then, SST increases rapidly and reaches its peak value at 14:00 CST when the SST is $0.50\text{ }^{\circ}\text{C}$ higher than the daily mean value.

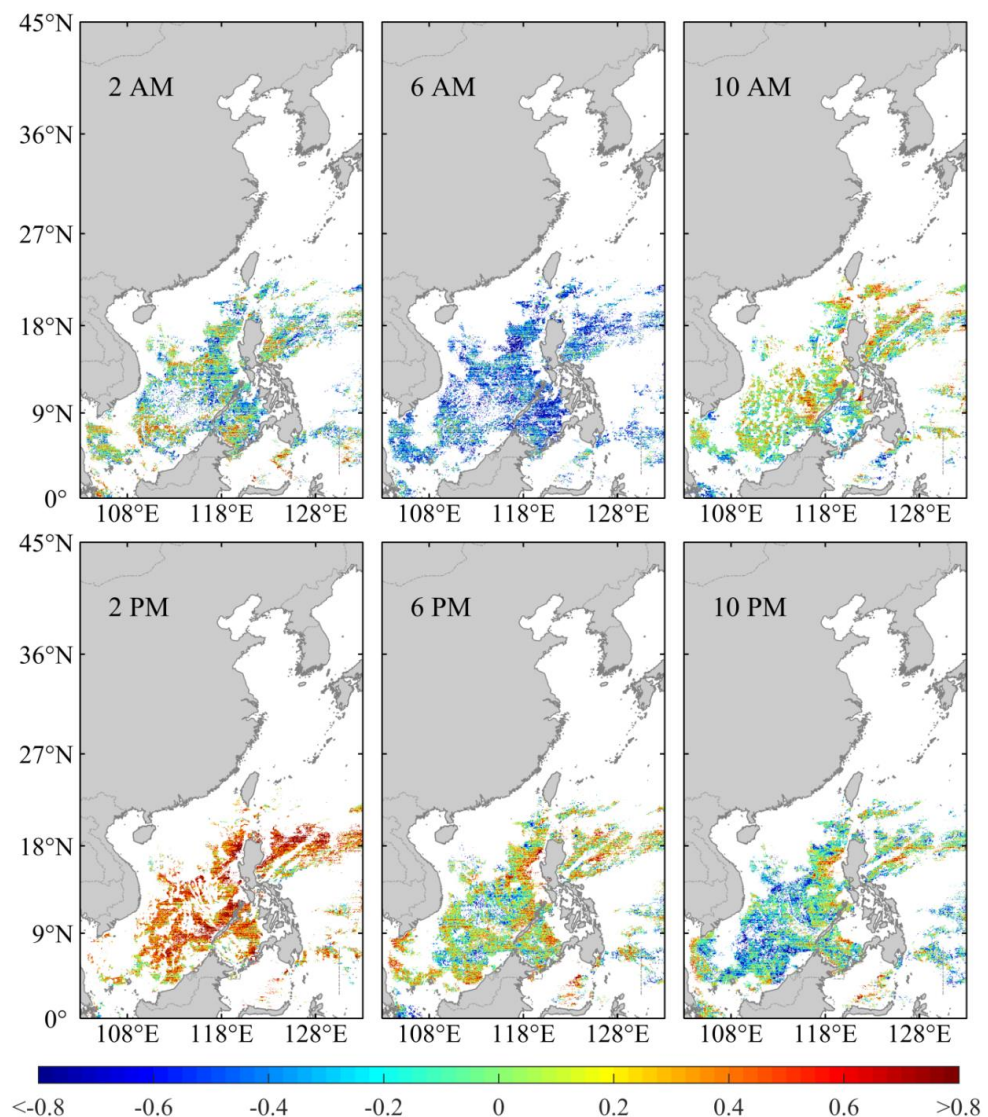


Figure 3. SST diurnal variation (SST_{dv}) at different hours on 9 February 2019 in the study area. The colors indicate the difference ($^{\circ}\text{C}$) between instantaneous SST and the daily mean SST. These SST data are from level-2 products of FY-4A/AGRI. The blank areas in the figure are missing data due to cloud pollution.

Because of the strong influence of clouds, the SST valid data cannot cover the whole study area on any single day during the study period from June 2018 to May 2019. We thus mapped the monthly mean SST at different time of a day in October 2018 to provide a more detail insight to the diurnal variability of SST (Figure 4). Meanwhile, the maximum amplitude (SST_{amp_max}) of SST daily variation is defined by the difference between the daily maximum and minimum of SST and the monthly mean SST_{amp_max} in $1^\circ \times 1^\circ$ grid are presented in Figure 4b.

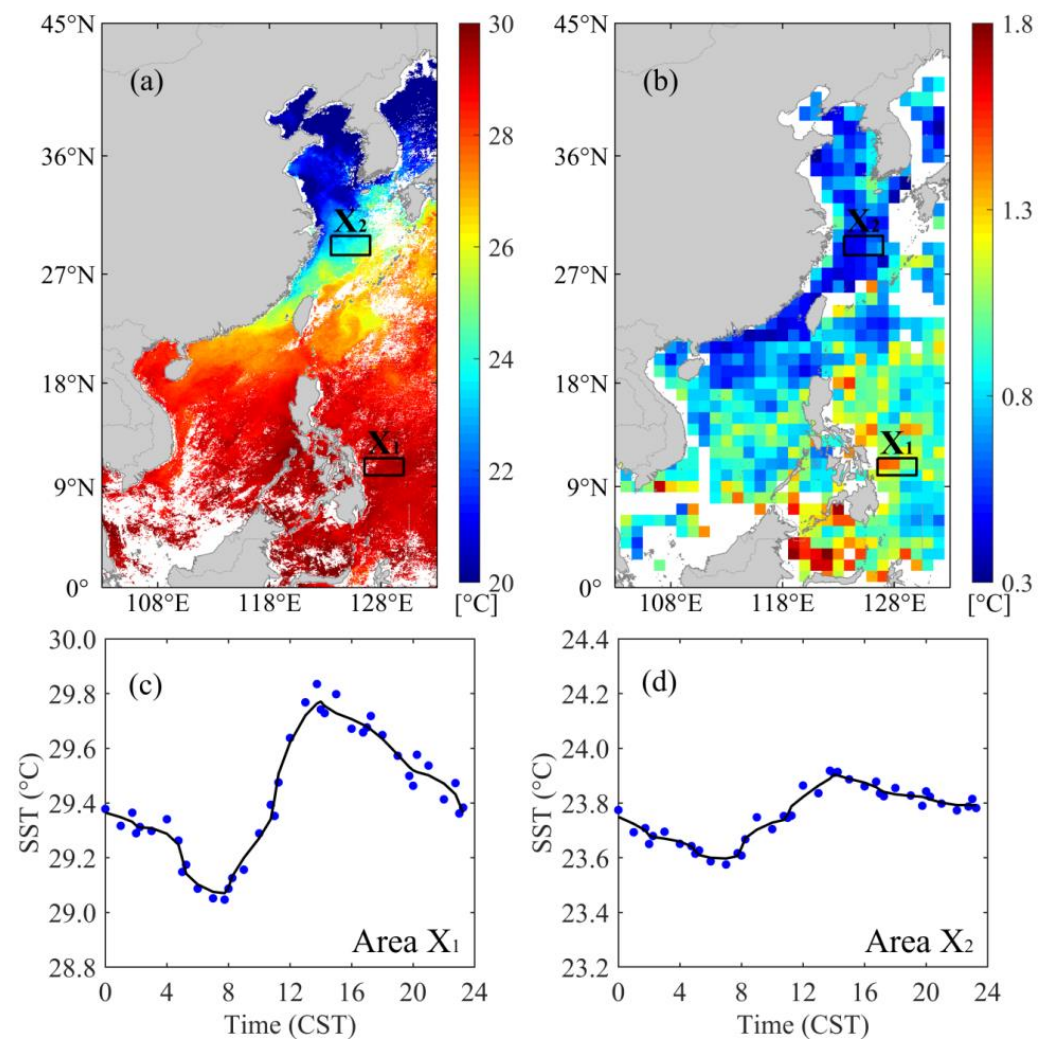


Figure 4. (a) The monthly mean SST ($^\circ\text{C}$) and (b) the monthly mean values of SST_{amp_max} in bins of $1^\circ \times 1^\circ$ ($^\circ\text{C}$) during October 2018 in China seas. The SST_{amp_max} is the maximum difference of SST in a day. Time series of SST diurnal variation in area X_1 (c) and area X_2 (d) in October 2018. The blue dots are monthly mean values of SST ($^\circ\text{C}$) for each hour and the black line is the trendline obtained by smoothing the scatters.

The results show decrease in both of the monthly mean and diurnal variability of SST with the increase in latitude (Figure 4a,b). The south region X_1 and north region X_2 are thus selected to display the difference in SST at different latitudes. Although the mean SST in region X_1 (29.4°C) is higher than that in region X_2 (23.8°C), the diurnal variations of SST in the regions have a similar tendency. It shows a sinusoidal form which reaches the diurnal minimum at 7:00 CST and then rising rapidly, achieving the maximum at 14:00 CST. In spite of this, the amplitude of SST diurnal variation in region X_1 (0.79°C) is greater than that in region X_2 (0.34°C). This characteristic is consistent with satellite observations and model results in Gentemann, et al. [44] and it may be affected by insolation and sea surface wind speed [45,46]. Because of the low wind speed (4 m/s) and the high solar

radiation (850 W/m^2) in region X_1 (Figure A1d,h), the heat accumulates at the sea surface, resulting in great diurnal variation of SST [47]. In contrast, the strong wind speed (8 m/s) dominates the SST diurnal variation when the insolation is weak (580 W/m^2) in region X_2 (Figure A1d,h). It causes convergent currents and transfers heat from the surface to the deeper water, which slows down sea surface warming and leads to small magnitude of SST diurnal variability [48]. Therefore, the amplitude of diurnal SST variation in region X_1 is greater than that in region X_2 .

3.2. Diurnal Variation of SST

According to the latitude, the study area is divided into three zones: $0\text{--}15^\circ\text{N}$ is the first zone (denoted as Zone 1), $15\text{--}30^\circ\text{N}$ is the second zone (denoted as Zone 2) and $30\text{--}45^\circ\text{N}$ is the third zone (denoted as Zone 3). Meanwhile, January, April, July and October represent winter, spring, summer and fall respectively. As presented in Figure 5a–c, Zone 3 exhibits the most significant seasonal variation of SST (up to 15°C), with an average SST of 27.06°C in summer, 20.96°C in autumn, 12.99°C in spring and 12.11°C in winter. In comparison, the seasonal variation of SST in Zone 1 is the smallest ($<3.00^\circ\text{C}$). In this region, SST in spring, summer and autumn is between 29.00°C and 30.00°C , while that in winter is around 27.58°C . On average, SST in the three zones is the highest in summer and the lowest in winter. Figure 5d–f shows that the time series of SST_{dv} in each zone in different seasons have similar sinusoidal patterns, with the minimum value at 06:00–08:00 CST and the maximum value at 13:00–15:00 CST. It can be seen from this figure that the SST_{dv} in Zone 1 is maximum in autumn (0.65°C) and is similar and minimum in winter and summer (0.33°C). Zone 2 has the largest SST_{dv} in summer (0.60°C), followed by spring (0.49°C) and autumn (0.41°C), while the smallest SST_{dv} in winter (0.38°C). In the meantime, the maximum SST_{dv} (0.92°C) in Zone 3 appears in winter and the minimum (0.34°C) appears in autumn.

Figure 6 presents the time series of SST_{dv} in different zones for season wise. In winter, it demonstrates that Zone 3 has the largest SST_{dv} (0.92°C , which is the difference between the maximum of 0.44°C and the minimum of -0.48°C), while Zone 1 and Zone 2 have similar variation (0.32°C and 0.38°C). In spring, the cycles of SST_{dv} in the three zones are similar and their variation amplitudes are close to 0.49°C . In summer, the magnitude of SST_{dv} increased from 0.33°C in Zone 1 to 0.73°C in Zone 3, revealing the rule of gradual increase from south to north. On the contrary, the amplitude of SST_{dv} gradually decreases from south (0.65°C) to north (0.34°C) in autumn.

Previous researchers have thoroughly validated that the diurnal variability of SST is positively correlated with solar radiation and negatively correlated with wind speed on sea surface [44–46]. Therefore, we guess that the features of SST_{dv} in Figure 6 may be the results of combined effects of sea surface wind speed and solar radiation. In winter (Figure A1a,e), the wind speed in the north and south of the study area is similar (9.5 m/s). The solar radiation in Zone3 (350 W/m^2) is significantly lower than that in Zone1 (700 W/m^2) and Zone2 (550 W/m^2), for the Sun is directly above the Southern Hemisphere. As a result, the magnitude of SST_{dv} in Zone3 is greater than that in other zones. In spring (Figure A1b,f), as the subsolar point moves to the equator, the difference of solar radiation between the north and south of the study area is reduced and their wind speed is similar, so the amplitudes of SST_{dv} in the three regions are alike. In summer (Figure A1c,g), the solar radiation are roughly the same (750 W/m^2) in the whole study area, while the sun is directly above a point near the tropic of cancer. The wind speed in the south (8 m/s) is stronger than that in the north (5 m/s), resulting in the gradual decrease of SST_{dv} from south to north opposite to the wind speed. In autumn (Figure A1d,h), the direct point of the sun moves to the equator again, the solar radiation decreases from south (800 W/m^2) to north (500 W/m^2) while the wind speed increases (from 3.5 m/s to 8.5 m/s), leading to the decrease of SST_{dv} from south to north.

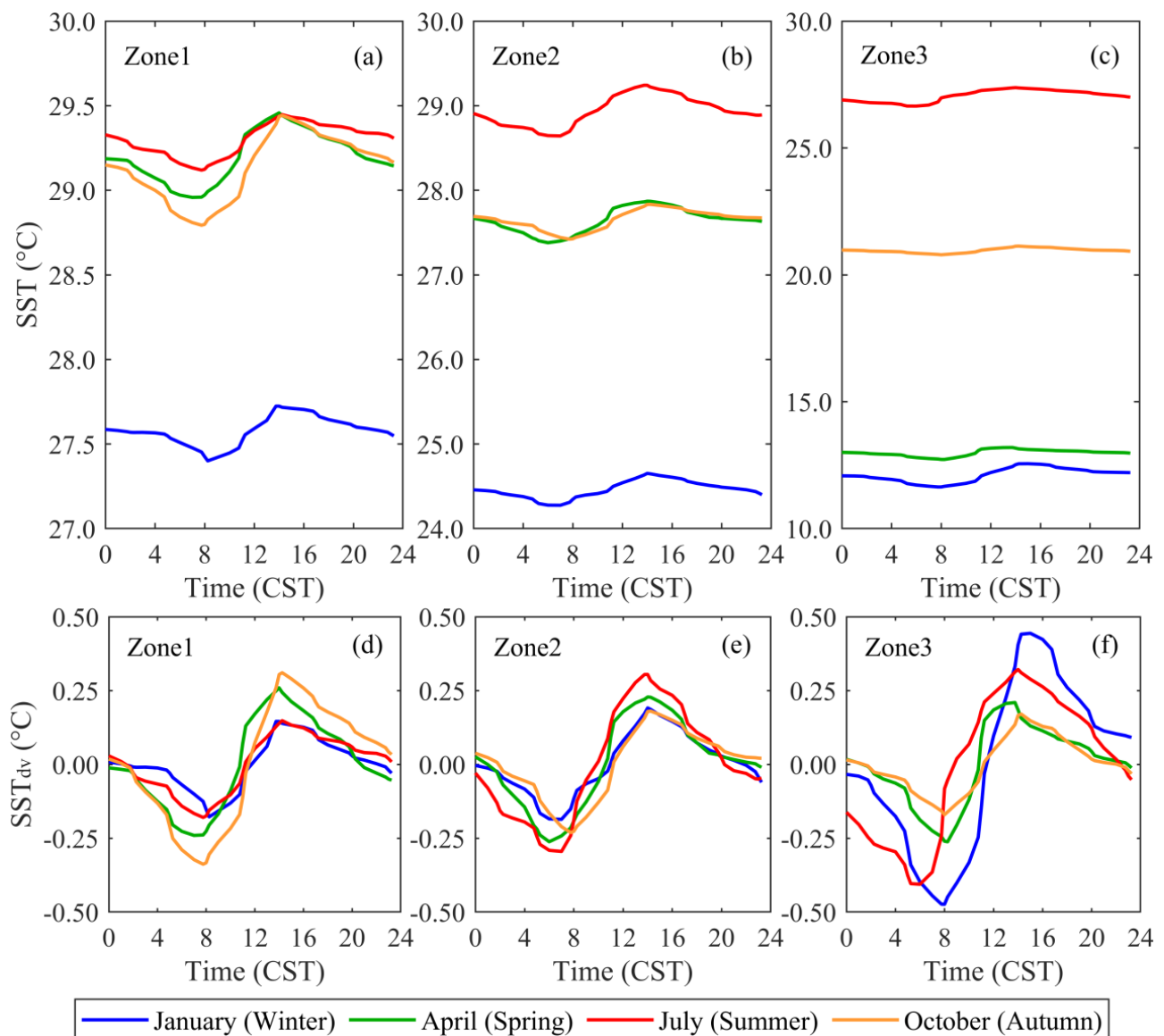


Figure 5. Time series of monthly mean SST (a–c) and monthly mean SST_{dv} (d–f) in January, April, July and October (representing winter, spring, summer and autumn, respectively) for the three zones. SST_{dv} (°C) = SST_i – SST_{daily_mean}, where *i* represents different hours. Zone 1 includes 0–15°N and Zone 2 includes 15–30°N, while Zone 3 includes 30–45°N.

3.3. Retrieval of Daily Mean SST

The polar orbiting satellite S-NPP passes through a given region only twice a day; therefore, the VIIRS sensor on it can only obtain instantaneous SST at 1–2 moments in China seas. If the instantaneous data are applied as its daily average SST products, the results will be larger or smaller than the actual values. As shown in Figure 7, the instantaneous SST obtained by VIIRS in Zone 2 on 25 June 2018 is 29.07 °C and the daily mean SST obtained by AGRI is 28.50 °C, which reveals an overestimate of 0.57 °C using instantaneous SST as daily mean. This result may lead to underestimation of latent heat flux in the numerical model during daytime and overestimation at night [22], resulting in errors in the estimation of sea surface energy balance [49]. Furthermore, the phase structure error appears in the simulation of seasonal variation of sea surface heat flux in the western Pacific warm pool, which reduces the accuracy of the air-sea oscillator coupling model for the ENSO [23].

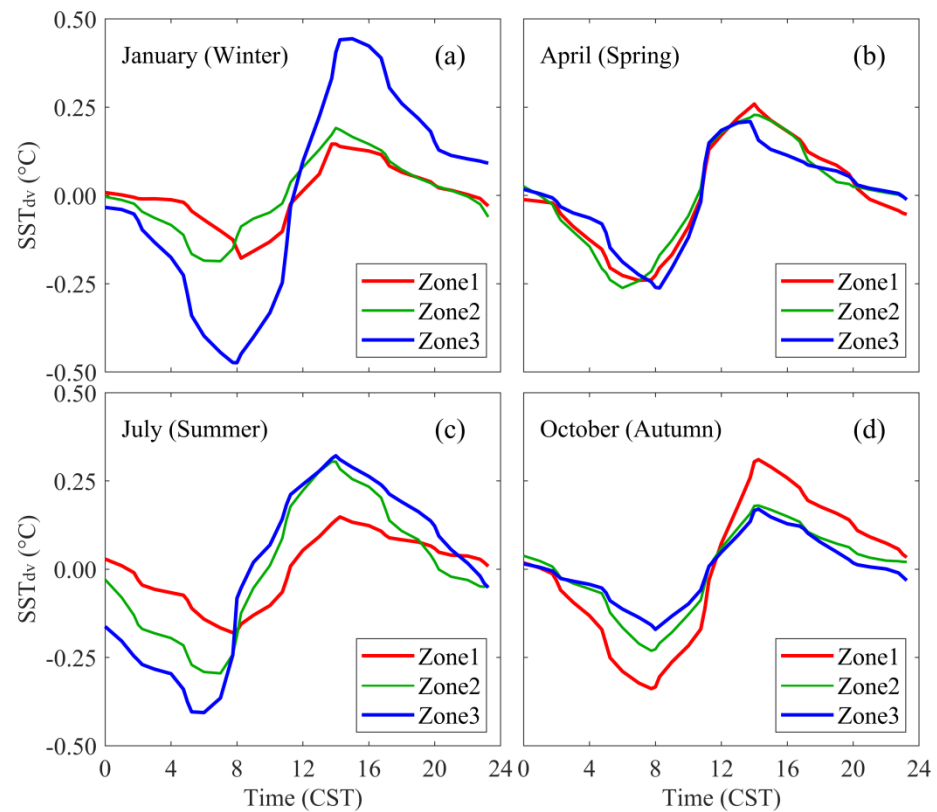


Figure 6. (a–d) Time series comparison of monthly mean SST_{dv} ($^{\circ}C$) for the three zones (January, April, July and October represent winter, spring, summer and autumn, respectively). It shows the diurnal range of SST and the time of extreme SST in different zones during the same month.

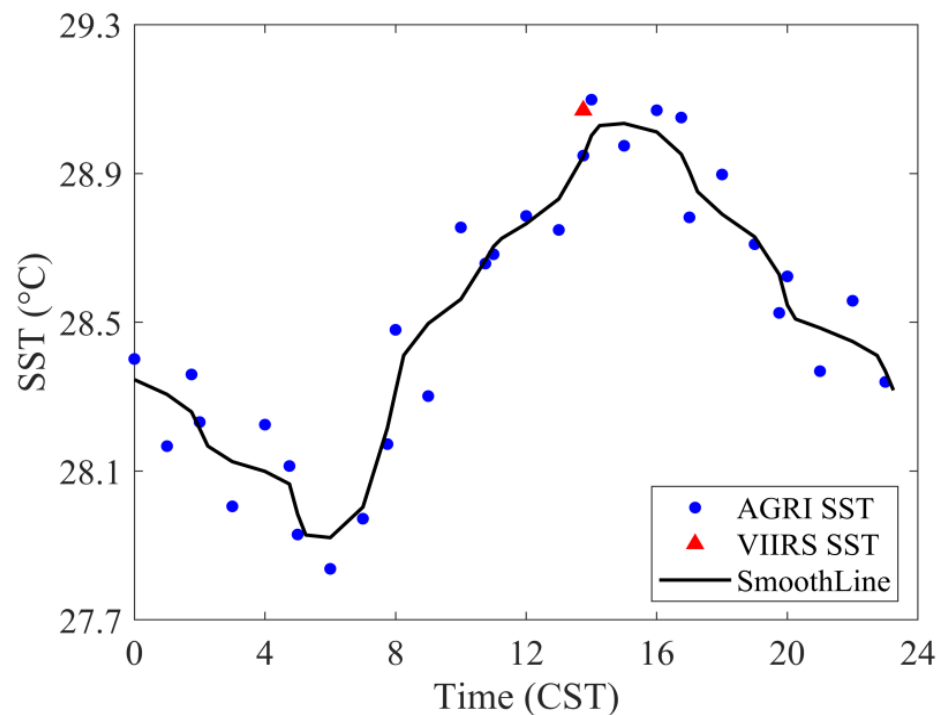


Figure 7. Diurnal variation of AGRI SST (blue dots) and VIIRS SST (red triangles) in Zone 2 on 25 June 2018. VIIRS SST was obtained by the sensor aboard S-NPP at approximately 13:30 p.m. (ascending node). The solid black line is time series curve of AGRI SST for the day, which is smoothed from the scatters.

The features of diurnal SST variation have been derived based on AGRI SST with high temporally resolution and the results can be used to retrieve the daily mean VIIRS SST products. Firstly, we calculated the daily mean AGRI SST and the instantaneous AGRI SST of 13:45 CST in each month. Secondly, the ratio (assuming K) of these two variables is taken as the retrieval coefficient of VIIRS SST. The retrieved daily mean VIIRS SST thus can be obtained as:

$$\frac{VIIRS_{dm}}{VIIRS_{ins}} = \frac{AGRI_{dm}}{AGRI_{ins}} = K \quad (1)$$

$$VIIRS_{dm} = K \times VIIRS_{ins} \quad (2)$$

where $VIIRS_{dm}$ and $VIIRS_{ins}$ represent the daily mean and instantaneous VIIRS SST, respectively, while $AGRI_{dm}$ and $AGRI_{ins}$ represent the daily mean and instantaneous values of AGRI SST, respectively.

The look-up table for retrieved coefficient K in each month is calculated from AGRI SST products (Table 1). The resultant K ranges from 0.960 to 0.990 in China seas. After retrieval, we are expected to obtain more accurate daily mean VIIRS SST.

Table 1. Lookup table of retrieval coefficient K for monthly mean of VIIRS SST.

Month	Zone 1	Zone 2	Zone 3
January	0.978	0.981	0.985
February	0.984	0.984	0.964
March	0.983	0.983	0.985
April	0.982	0.980	0.981
May	0.982	0.984	0.984
June	0.984	0.985	0.985
July	0.986	0.983	0.979
August	0.984	0.983	0.985
September	0.982	0.984	0.986
October	0.977	0.984	0.989
November	0.981	0.980	0.989
December	0.977	0.980	0.987

3.4. Verification of Retrieved Results

Figure 8 takes October 2018 and May 2019 as examples for the validation of the retrieval method for daily mean SST data in this paper. In May 2019, the daytime VIIRS SST has a RMSE of 0.595 °C and a bias of 0.522 °C as compared to daily mean AGRI SST. After applied retrieval method, the correlation coefficient between these two SST products remains unchanged ($R = 0.995$), while the RMSE decreases to 0.272 °C and the bias decreases to 0.007 °C. In October 2018, the RMSE is 0.627 °C and the bias is 0.552 °C between the daytime VIIRS SST and the daily mean AGRI SST. By contrast, the retrieved daily mean VIIRS SST has a RMSE of 0.284 °C and a bias of 0.005 °C with the daily mean AGRI SST. These results show that the retrieved VIIRS SST values are closer to the daily mean SST values, which is of great significance to the process of marine numerical simulation.

In the scatter plot of Figure 9, the daytime VIIRS SST and the retrieved daily mean VIIRS SST in the three zones are compared with the daily mean AGRI SST during the period between June 2018 and May 2019. After retrieval, the RMSE between daily mean VIIRS SST and daily mean AGRI SST is 0.123 °C in Zone 1, 0.131 °C in Zone 2 and 0.144 °C in Zone 3, while their correlation coefficients are more than 0.990. Meanwhile, it illustrates that the lower latitude has the better effect of retrieval, which might be related to the range of SST in different sea areas. It is concluded that the average RMSE of the three zones is 0.133 °C and the retrieval method of daily mean SST in this paper is feasible and practical.

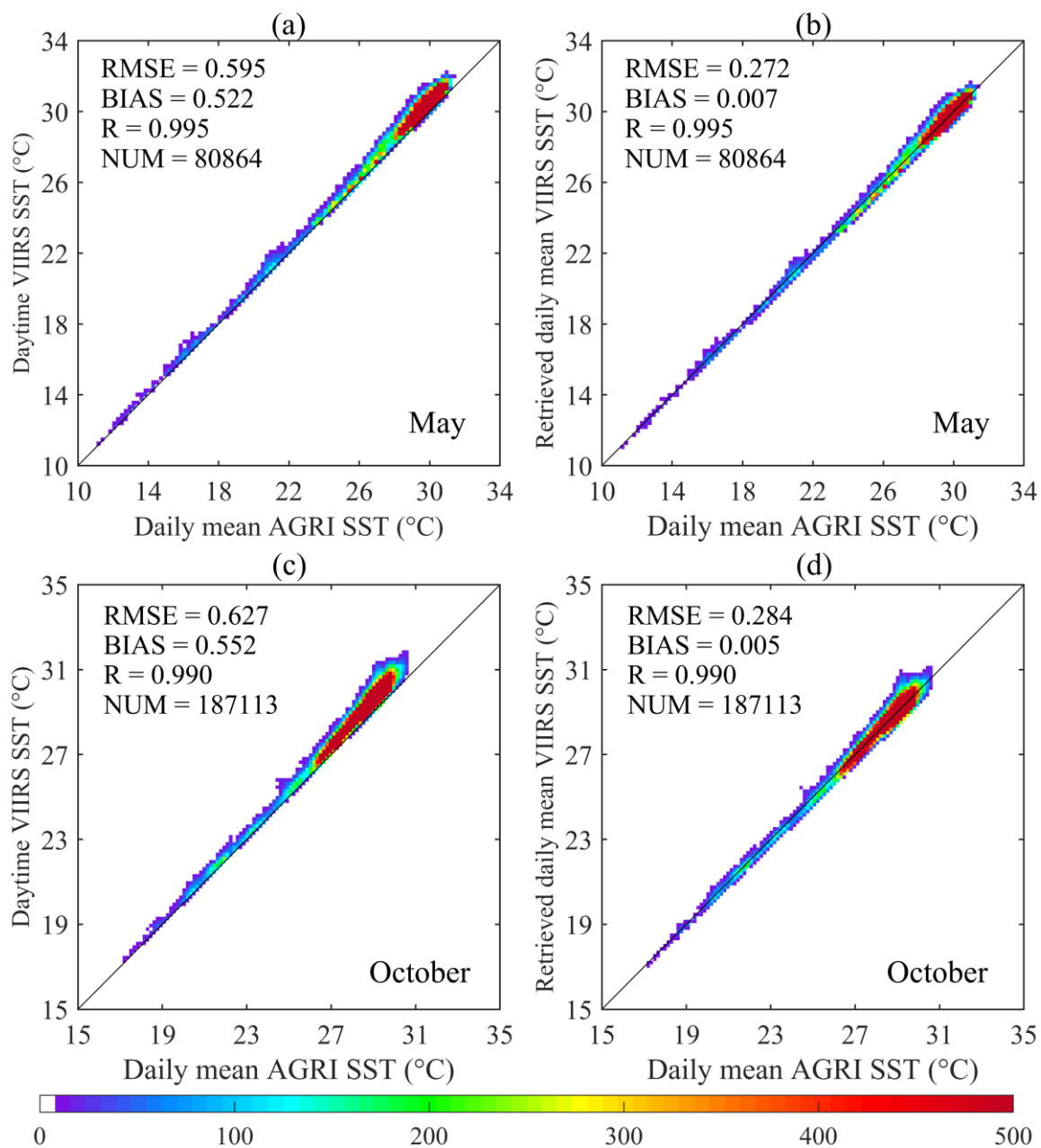


Figure 8. (a–d) Validation for retrieval of daily mean SST in the study area, while the spatiotemporal consistent daily means of AGRI SST are applied for comparison with the daytime VIIRS SST (**left panels**) and retrieved daily mean VIIRS SST (**right panels**) on October 2018 and May 2019.

Figure 10 presents the comparison of daily mean AGRI SST, instantaneous VIIRS SST in daytime, retrieved VIIRS SST and the mean of instantaneous VIIRS SST between day and night during July 2018. It shows that the instantaneous VIIRS SST data during daytime are about 0.50 °C higher than the daily mean of AGRI SST. After retrieval, the daily mean VIIRS SST is closer to the actual value and it indicates that the retrieval method in this paper can obtain more accurate daily mean SST data. In general, the daily mean is the arithmetic average of day and night, so we add instantaneous SST at night to better demonstrate the feasibility of this retrieval method. As can be seen from the Figure 10, the mean of instantaneous VIIRS SST between day and night still have a bias (about 0.14 °C) compared with the daily mean of AGRI SST, while the retrieved VIIRS SST data are very closer to it. This proves that the retrieval method in this paper can get accurate daily mean SST products and has certain necessity and reliability.

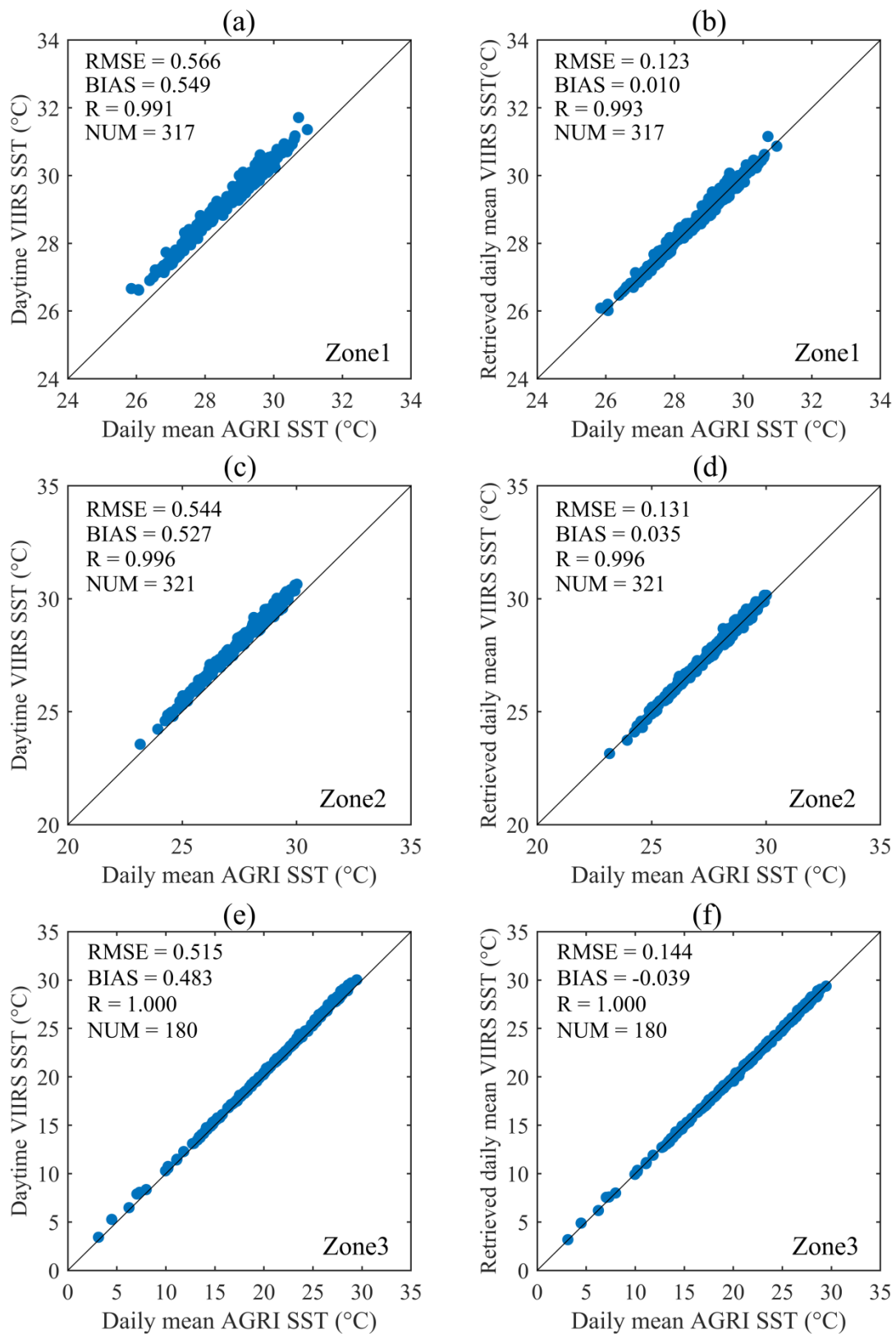


Figure 9. (a–f) Validation for retrieved results of daily mean SST in the three zones from June 2018 to May 2019, while the spatiotemporal consistent daily means of AGRI SST are applied for comparison with the daytime VIIRS SST (left panels) and retrieved daily mean VIIRS SST (right panels).

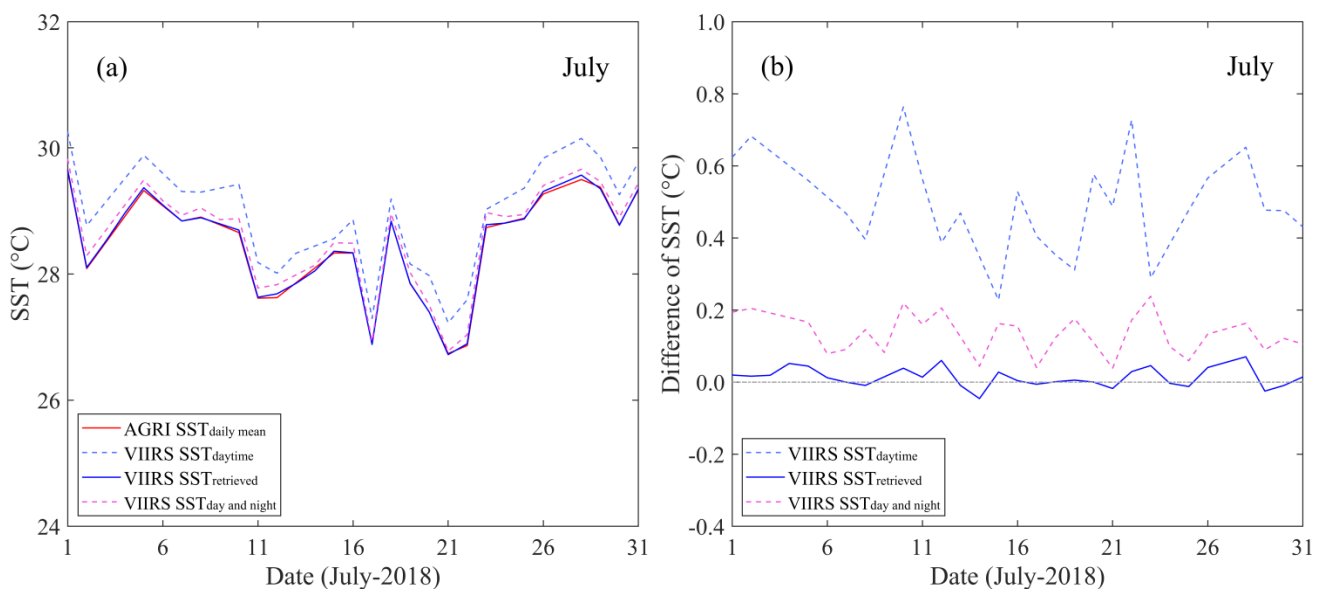


Figure 10. (a) Time series curves of daily mean AGRI SST (solid red curve), instantaneous SST of VIIRS during daytime (dashed blue curve), retrieved VIIRS SST (solid blue curve) and the mean of instantaneous VIIRS SST between day and night (dashed pink curve), during July 2018. (b) The difference between the other three kinds of SST in (a) and the daily mean of AGRI SST.

4. Discussion

Based on the analysis of FY-4A/AGRI SST data, it can be seen that SST in Chinese seas varies within a day and its pattern of diurnal variation is nearly a sinusoidal form, with the maximum value at 13:00–15:00 CST and the minimum value at 6:00–8:00 CST. This feature is consistent with the results from Gentemann, et al. [44] and Li, et al. [50]. This is due to the gradual accumulation of heat on the sea surface during the day, leading to increase of SST [51]. Although solar radiation peaks at about midday, the sea water absorbs more heat than it loses at this moment and it takes 1–3 h to reach thermal equilibrium. Then, SST decreases when the received heat from insolation weakens and no longer overcomes the heat losses due to sea surface latent and sensible heat fluxes [52]. Therefore, the daily peak of SST appears at 13:00–15:00 CST. At night, there is no solar radiation reaching sea surface [51] and the heat gained in daytime is lost to the atmosphere through latent and sensible heat fluxes, or penetrates into the deeper ocean through vertical mixing of sea water [53]. Thus, SST decreases gradually before sunrise and the diurnal minimum occurs at 6:00–8:00 CST. These facts indicate that SST is different at different times of the day and instantaneous SST values are not the same with daily mean SST values.

In order to obtain accurate daily mean SST products, researchers have tried many methods [45,49,54,55], including the fusion of multiple satellite data and the establishment of estimation model for diurnal SST variability. If we average instantaneous SST values of a polar-orbiting satellite when it crosses the ascending and descending node, the results will be closer to the daily mean SST than the instantaneous SST in daytime (Figure 10). However, for the influence of clouds, there are few pixels with effective values in both day and night, resulting in many blanks in the images of daily mean SST. At present, the Group for High Resolution Sea Surface Temperature (GHRSSST) provides daily SST fusion products merged from a variety of sensors and they are widely used in oceanographic researches. As the spatial resolution of different satellite data is inconsistent, the maximum spatial resolution of SST fusion products from GHRSSST is only 4 km, resulting in some SST information being smoothed. Meanwhile, the purpose of GHRSSST is to provide foundation SST and they reject SST data when the diurnal amplitude is larger than 3 K or the wind speed is less than 6 m/s in daytime, to prevent pollution caused by daily warming [54]. Thus, GHRSSST products cannot represent the true daily mean of SST. In addition, the workload of multi-data fusion is heavy, because the storage and processing for each satellite data type consumes memory

and time. Therefore, it is little feasible to obtain daily mean SST data through satellite data fusion. At this time, various estimation models for SST diurnal variation are established by utilization of solar radiation, sea surface wind speed, precipitation and other data [45,48,49]. It is challenging to obtain high frequency observations of wind speed and precipitation in a large area and there are many boundary conditions and limitations exist to the estimation models. In consequence, it is difficult to obtain accurate daily mean SST data through the estimation model of SST_{dv} . We propose a new method to obtain the relationship between instantaneous value and daily mean value as retrieval coefficient through the diurnal cycle of SST and then retrieve the daily mean SST products of polar-orbiting satellite. By this method, the spatial resolution of the daily mean SST products is consistent with that of daytime VIIRS SST. Since the recently launched FY-4A/AGRI sensor can obtain continuous observations of SST within 24 h and the data are relatively easy to achieve [36], it is feasible to apply them to retrieve SST products of polar-orbiting satellites.

Whereas, a one-year data of AGRI from June 2018 to May 2019 are just utilized to analyze the temporal and spatial characteristics of SST diurnal variations in China seas. In fact, the diurnal variation of SST may also have interannual variation and the coefficient lookup table in this study may lead to bias for results from other years. Therefore, more works will be done for universal method by use of longer time data set.

5. Conclusions

The existing SST daily products from polar-orbiting satellites are in fact instantaneous SST measurements at the time of satellite transit and they cannot represent the actual daily mean SST. In this paper, geostationary satellite data of FY-4A/AGRI are applied to learn that the diurnal SST variations have different amplitudes in different seasons and latitudes in China seas, but they show a similar diurnal variability in sinusoidal form with the maximum value at 13:00–15:00 CST and the minimum value at 6:00–8:00 CST. According to this regularity, a lookup table of coefficients for the retrieval of SST daily products is established and its values range from 0.960 to 0.990. After the retrieval of 7716 images, it is found that the retrieval of daily mean SST has an average RMSE of 0.133 °C. It proves the feasibility and reliability of using geostationary satellite data to retrieve the daily mean SST products from polar-orbit satellites. Based on this idea, available data can be provided for some applications which need daily mean SST, weekly mean SST and monthly mean SST.

In the future, there will be a lot of work to be done as more and more AGRI data are continually accumulated. For example, the diurnal variation characteristics of SST in China seas over a longer time series will be analyzed with the use of more than three years data. The zones within the research area will be divided more finely and the retrieval coefficient lookup table will be more detailed, which can further obtain more accurate retrieval results. This retrieval method will be extended to different remote sensing data and different sea areas to explore regional and global SST diurnal variation characteristics and get more high-quality daily mean SST products over the world.

Author Contributions: Conceptualization, C.C. and Q.L.; methodology, C.C. and Q.L.; validation, Q.L., Q.H. and C.C.; formal analysis, Q.L. and C.C.; writing—original draft preparation, Q.L.; writing—review and editing, Q.L., Q.H. and C.C.; funding acquisition, C.C. All authors have read and agreed to the published version of the manuscript.

Funding: This research was funded by the National Key Research and Development Project (2018YFC1406 604), the Key Special Project for Introduced Talents Team of Southern Marine Science and Engineering Guangdong Laboratory (Guangzhou) (GML2019ZD0305), the National Natural Science Foundation of China (U1901215, 41906026) and the Scientific Research Key Project from Guangzhou City (201707020031).

Acknowledgments: We are sincerely grateful to the Group for High-Resolution SST (GHRSSST) for the S-NPP/VIIRS NAVO SST level-2 products. We also express our sincere gratitude to the National Satellite Meteorological Center (NSMC) of China Meteorological Administration (CMA) for the FY-4A/AGRI level-1 products. The in situ SST products are obtained from the in situ SST Quality

Monitor system (iQuam) which is developed by NOAA. Moreover, we wish to thank Jie Wu, Weikang Zhan and Sravanthi Nukapothula for their insightful comments and suggestions, which have greatly improved this article.

Conflicts of Interest: The authors declare no conflict of interest.

Appendix A

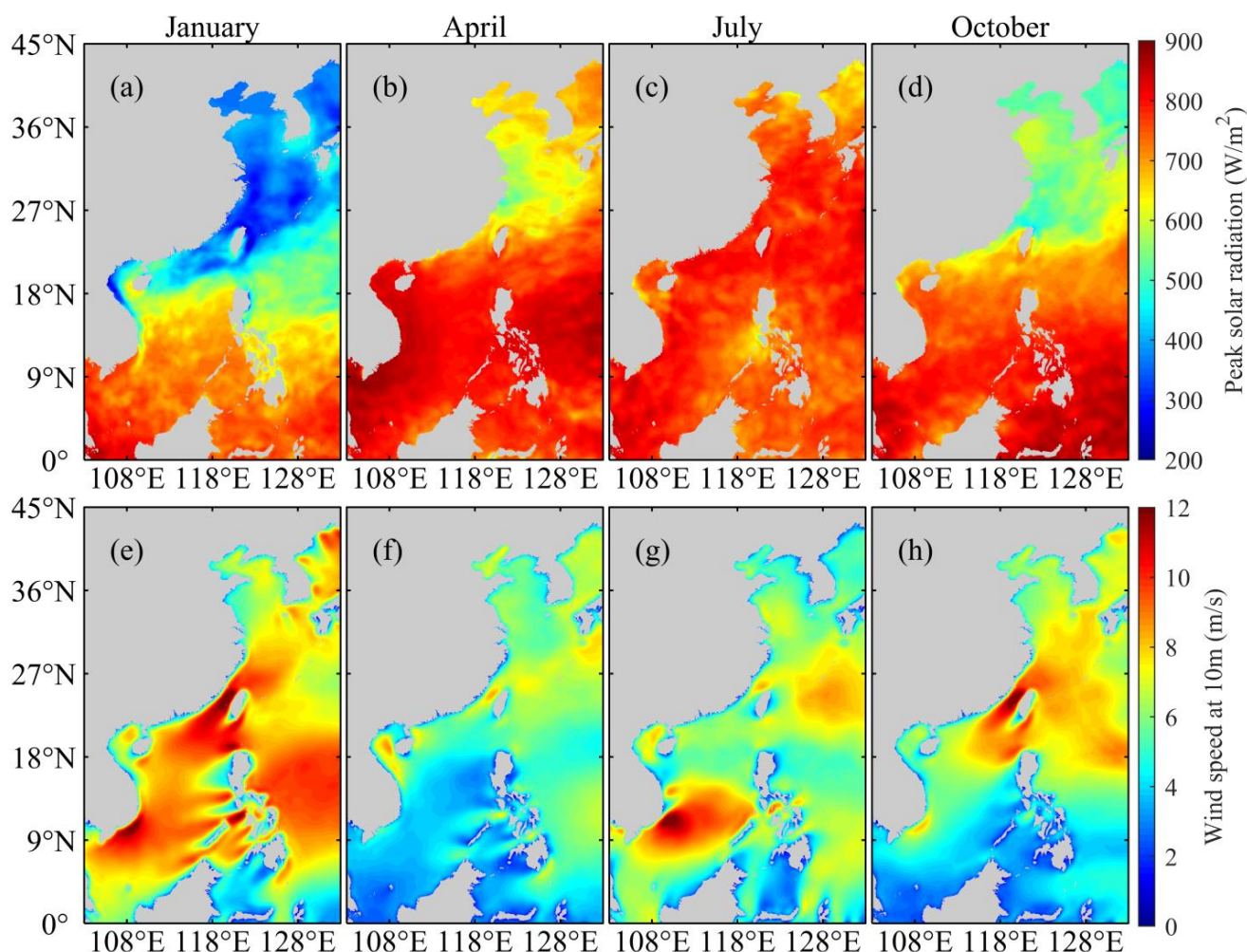


Figure A1. Distribution diagrams of peak solar radiation (a–d) and wind speed at 10 m surface (e–h) during different seasons in the study area (January, April, July and October represent winter, spring, summer and autumn respectively). These data are from the NCEP Climate Forecast System Version 2.

References

1. Kawai, Y.; Wada, A. Diurnal Sea Surface Temperature Variation and its Impact on the Atmosphere and Ocean: A Review. *J. Oceanogr.* **2007**, *63*, 721–744. [[CrossRef](#)]
2. Zaiss, J.; Boyd, P.W.; Doney, S.C.; Havenhand, J.N.; Levine, N. Impact of Lagrangian Sea Surface Temperature Variability on Southern Ocean Phytoplankton Community Growth Rates. *Glob. Biogeochem. Cycles* **2020**, *35*, 1–16. [[CrossRef](#)]
3. Santos, A.M.P. Fisheries Oceanography using Satellite and Airborne Remote Sensing Methods: A Review. *Fish. Res.* **2000**, *49*, 1–20. [[CrossRef](#)]
4. Chen, P.; Chen, X. Evaluating the Effects of Sea Surface Temperature Variations on Fishing Ground of Anchoveta (*Engraulis ringens*) in the Southeast Pacific Ocean. *Acta Oceanolog. Sin.* **2017**, *39*, 79–88.
5. Stuart-Menteth, A.C. A Global Study of Diurnal Warming using Satellite-derived Sea Surface Temperature. *J. Geophys. Res.* **2003**, *108*. [[CrossRef](#)]
6. Barton, B.I.; Lique, C.; Lenn, Y.D. Water Mass Properties Derived From Satellite Observations in the Barents Sea. *J. Geophys. Res. Oceans* **2020**, *125*, 1–18. [[CrossRef](#)]

7. Béréziat, D.; Herlin, I. *Coupling Dynamic Equations and Satellite Images for Modelling Ocean Surface Circulation*; Springer International Publishing: Cham, Switzerland, 2014; pp. 191–205.
8. Dutheil, C.; Lengaigne, M.; Bador, M.; Vialard, J.; Lefevre, J.; Jourdain, N.C.; Jullien, S.; Peltier, A.; Sultan, B.; Menkes, C. Impact of Projected Sea Surface Temperature Biases on Tropical Cyclones Projections in the South Pacific. *Sci. Rep.* **2020**, *10*, 4838. [[CrossRef](#)] [[PubMed](#)]
9. Varlas, G.; Katsafados, P.; Korres, G.; Papadopoulos, A. Assessing the Impact of Argo Floats Temperature Measurements on the Numerical Weather Prediction Forecast Skill. *Mediterr. Mar. Sci.* **2019**, *20*, 331–341. [[CrossRef](#)]
10. Chen, W.; Schulz-Stellenfleth, J.; Grayek, S.; Staneva, J. Impacts of the Assimilation of Satellite Sea Surface Temperature Data on Volume and Heat Budget Estimates for the North Sea. *J. Geophys. Res. Oceans* **2021**, *126*, 1–25. [[CrossRef](#)]
11. Hsu, P.-C.; Ho, C.-Y.; Lee, H.-J.; Lu, C.-Y.; Ho, C.-R. Temporal Variation and Spatial Structure of the Kuroshio-Induced Submesoscale Island Vortices Observed from GCOM-C and Himawari-8 Data. *Remote Sens.* **2020**, *12*, 883. [[CrossRef](#)]
12. Luo, B.; Minnett, P.J.; Nalli, N.R. Infrared Satellite-derived Sea Surface Skin Temperature Sensitivity to Aerosol Vertical Distribution—Field Data Analysis and Model Simulations. *Remote Sens. Environ.* **2021**, *252*, 112151. [[CrossRef](#)]
13. Yang, H.; Gao, Q.; Ji, H.; He, P.; Zhu, T. Sea Surface Temperature Data from Coastal Observation Stations: Quality Control and Semidiurnal Characteristics. *Acta Oceanolog. Sin.* **2019**, *38*, 31–39. [[CrossRef](#)]
14. Coppo, P.; Mastrandrea, C.; Stagi, M.; Calamai, L.; Nieke, J. The Sea and Land Surface Temperature Radiometer (SLSTR) Detection Assembly Design and Performance. *Proc. SPIE Int. Soc. Opt. Eng.* **2013**, *8889*, 888914-1.
15. Barton, I.J. Improving Satellite-Derived Sea Surface Temperature Accuracies Using Water Vapor Profile Data. *J. Atmos. Ocean. Technol.* **2011**, *28*, 85–93. [[CrossRef](#)]
16. Mittaz, J.; Harris, A. A Physical Method for the Calibration of the AVHRR/3 Thermal IR Channels. Part II: An In-Orbit Comparison of the AVHRR Longwave Thermal IR Channels on Board MetOp-A with IASI. *J. Atmos. Ocean. Technol.* **2010**, *28*, 1072–1087. [[CrossRef](#)]
17. Wick, G.A.; Bates, J.J.; Scott, D.J. Satellite and Skin-Layer Effects on the Accuracy of Sea Surface Temperature Measurements from the GOES Satellites. *J. Atmos. Ocean. Technol.* **2002**, *19*, 1834–1848. [[CrossRef](#)]
18. Hosoda, K. Global Space-time Scales for Day-to-day Variations of Daily-Minimum and Diurnal Sea Surface Temperatures: Their Distinct Spatial Distribution and Seasonal Cycles. *J. Oceanogr.* **2016**, *72*, 1–18. [[CrossRef](#)]
19. Stramma, L.; Cornillon, P.; Weller, R.A.; Price, J.F.; Briscoe, M.G. Large Diurnal Sea Surface Temperature Variability: Satellite and In Situ Measurements. *J. Phys. Oceanogr.* **1986**, *16*, 827–837. [[CrossRef](#)]
20. Flament, P.; Firing, J.; Sawyer, M.; Trefois, C. Amplitude and Horizontal Structure of A Large Sea Surface Warming Event During the Coastal Ocean Dynamics Experiment. *J. Phys. Oceanogr.* **1994**, *24*, 124–139.
21. Gentemann, C.L.; Minnett, P.J.; Le Borgne, P.; Merchant, C.J. Multi-satellite measurements of large diurnal warming events. *Geophys. Res. Lett.* **2008**, *35*, L22602. [[CrossRef](#)]
22. Zeng, X.; Dickinson, R.E. Impact of Diurnally-varying Skin Temperature on Surface Fluxes over the Tropical Pacific. *Geophys. Res. Lett.* **1998**, *25*, 1411–1414. [[CrossRef](#)]
23. Masson, S.; Terray, P.; Madec, G.; Luo, J.-J.; Yamagata, T.; Takahashi, K. Impact of Intra-daily SST Variability on ENSO Characteristics in A Coupled Model. *Clim. Dyn.* **2011**, *39*, 681–707. [[CrossRef](#)]
24. Clayson, C.A.; Bogdanoff, A.S. The Effect of Diurnal Sea Surface Temperature Warming on Climatological Air–Sea Fluxes. *J. Clim.* **2013**, *26*, 2546–2556. [[CrossRef](#)]
25. Huang, A.; Zhang, Y.; Wang, Z.; Wu, T.; Huang, D.; Zhou, Y.; Zhao, Y.; Huang, Y.; Kuang, X.; Zhang, L.; et al. Extended range simulations of the extreme snow storms over southern China in early 2008 with the BCC_AGCM2.1 model. *J. Geophys. Res. Atmos.* **2013**, *118*, 8253–8273. [[CrossRef](#)]
26. Achuthavarier, D.; Krishnamurthy, V. Role of Indian and Pacific SST in Indian Summer Monsoon Intraseasonal Variability. *J. Clim.* **2011**, *24*, 2915–2930. [[CrossRef](#)]
27. Ouellet, P.; Savard, L.; Larouche, P. Spring oceanographic conditions and northern shrimp *Pandalus borealis* recruitment success in the north-western Gulf of St. Lawrence. *Mar. Ecol. Prog. Ser.* **2007**, *339*, 229–241. [[CrossRef](#)]
28. Hartuti, M.; Tjahjaningsih, A.; Effendy, I.; Sitorus, J. Weekly sea surface temperature from SNPP-VIIRS data using open source software. *IOP C Ser. Earth Environ.* **2020**, *500*, 012064. [[CrossRef](#)]
29. Wolfe, R.E.; Lin, G.; Nishihama, M.; Tewari, K.P.; Tilton, J.C.; Isaacman, A.R. Suomi NPP VIIRS prelaunch and on-orbit geometric calibration and characterization. *J. Geophys. Res. Atmos.* **2013**, *118*, 11508–11521. [[CrossRef](#)]
30. Chirokova, G.; Demaria, R.; Dostalek, J.F.; Beven, D.J.L. Improving Tropical Cyclone Track and Intensity Forecasting with JPSS imager and Sounder Data. In Proceedings of the 31st Conference on Hurricanes and Tropical Meteorology 2014 American Meteorological Society, San Diego, CA, USA, 31 March–4 April 2014.
31. Minnett, P.J.; Evans, R.H.; Podestá, G.P.; Kilpatrick, K.A. Sea-Surface Temperature from Suomi-NPP VIIRS: Algorithm Development and Uncertainty Estimation. In Proceedings of the SPIE-The International Society for Optical Engineering, Baltimore, MD, USA, 5–9 May 2014; p. 91110C.
32. Xiong, X.; Butler, J.; Wu, A.; Chiang, K.V.; Efremova, B.; Madhavan, S.; Mcintire, J.; Oudrari, H. Comparison of MODIS and VIIRS Onboard Blackbody Performance. In Proceedings of the Sensors, Systems, and Next-Generation Satellites XVI, Edinburgh, UK, 24–27 September 2012.

33. Tu, Q.; Pan, D.; Hao, Z. Validation of S-NPP VIIRS Sea Surface Temperature Retrieved from NAVO. *Remote Sens.* **2015**, *7*, 17234–17245. [[CrossRef](#)]
34. Cayula, J.-F.P.; May, D.A.; McKenzie, B.D.; Willis, K.D. VIIRS-derived SST at the Naval Oceanographic Office: From evaluation to operation. In Proceedings of the SPIE, Ocean Sensing and Monitoring V, Baltimore, MD, USA, 29 April–3 May 2013.
35. Zhang, P.; Zhu, L.; Tang, S.; Gao, L.; Chen, L.; Zheng, W.; Han, X.; Chen, J.; Shao, J. General Comparison of FY-4A/AGRI With Other GEO/LEO Instruments and Its Potential and Challenges in Non-meteorological Applications. *Front. Earth Sci.* **2019**, *6*, 1. [[CrossRef](#)]
36. Yang, J.; Zhang, Z.; Wei, C.; Lu, F.; Guo, Q. Introducing the New Generation of Chinese Geostationary Weather Satellites, Fengyun-4. *Bull. Am. Meteorol. Soc.* **2017**, *98*, 1637–1658. [[CrossRef](#)]
37. Wang, G.; Shen, X. The FY-4 Radiometer Imager and the Application of its Data in the Satellite Meteorology. *Chin. J. Nat.* **2018**, *40*, 1–11.
38. Walton, C.C.; Pichel, W.G.; Sapper, J.F.; May, D.A. The Development and Operational Application of Nonlinear Algorithms for the Measurement of Sea Surface Temperatures with the NOAA Polar-orbiting Environmental Satellites. *J. Geophys. Res. Oceans* **1998**, *103*, 27999–28012. [[CrossRef](#)]
39. Xu, F.; Ignatov, A. In situ SST Quality Monitor (iQuam). *J. Atmos. Ocean. Technol.* **2014**, *31*, 164–180. [[CrossRef](#)]
40. Ingleby, B.; Huddleston, M. Quality Control of Ocean Temperature and Salinity Profiles-Historical and Real-time Data. *J. Mar. Syst.* **2007**, *65*, 158–175. [[CrossRef](#)]
41. Tu, Q.; Pan, D.; Hao, Z.; Chen, J. Observations of SST diurnal variability in the South China Sea. In Proceedings of the Remote Sensing of the Ocean, Sea Ice, Coastal Waters, and Large Water Regions 2015, Toulouse, France, 21–24 September 2015; p. 963800.
42. Dash, P.; Ignatov, A.; Kihai, Y.; Sapper, J. The SST Quality Monitor (SQUAM). *J. Atmos. Ocean. Technol.* **2010**, *27*, 1899–1917. [[CrossRef](#)]
43. Song, D.; Duan, Z.; Zhai, F.; He, Q. Surface diurnal warming in the East China Sea derived from satellite remote sensing. *J. Oceanol. Limnol.* **2018**, *36*, 620–629. [[CrossRef](#)]
44. Gentemann, C.L.; Donlon, C.J.; Stuart-Menteth, A.; Wentz, F.J. Diurnal signals in satellite sea surface temperature measurements. *Geophys. Res. Lett.* **2003**, *30*, 1140. [[CrossRef](#)]
45. Yan, Y.; Wang, G.; Chen, C.; Ling, Z. Annual and Semiannual Cycles of Diurnal Warming of Sea Surface Temperature in the South China Sea. *J. Geophys. Res. Oceans* **2018**, *123*, 5797–5807. [[CrossRef](#)]
46. Zhang, H.; Beggs, H.; Wang, X.H.; Kiss, A.E.; Griffin, C. Seasonal patterns of SST diurnal variation over the Tropical Warm Pool region. *J. Geophys. Res. Oceans* **2016**, *121*, 8077–8094. [[CrossRef](#)]
47. Wirasatriya, A.; Kawamura, H.; Shimada, T.; Hosoda, K. Climatology of hot events in the western equatorial Pacific. *J. Oceanogr.* **2014**, *71*, 77–90. [[CrossRef](#)]
48. Wirasatriya, A.; Hosoda, K.; Setiawan, J.D.; Susanto, R.D. Variability of Diurnal Sea Surface Temperature during Short Term and High SST Event in the Western Equatorial Pacific as Revealed by Satellite Data. *Remote Sens.* **2020**, *12*, 3230. [[CrossRef](#)]
49. Webster, P.J.; Clayson, C.A.; Curry, J.A. Clouds, Radiation, and the Diurnal Cycle of Sea Surface Temperature in the Tropical Western Pacific. *J. Clim.* **1996**, *9*, 1712–1730. [[CrossRef](#)]
50. Li, X.; Ling, T.; Zhang, Y.; Zhou, Q. A 31-year Global Diurnal Sea Surface Temperature Dataset Created by an Ocean Mixed-Layer Model. *Adv. Atmos. Sci.* **2018**, *35*, 1443–1454. [[CrossRef](#)]
51. Guemas, V.; Salas-Méla, D.; Kageyama, M.; Giordani, H.; Voltaire, A. Impact of the ocean diurnal cycle on the North Atlantic mean sea surface temperatures in a regionally coupled model. *Dyn. Atmos. Oceans* **2013**, *60*, 28–45. [[CrossRef](#)]
52. Zhu, X.; Minnett, P.J.; Berkemans, R.; Hendee, J.; Manfrino, C. Diurnal warming in shallow coastal seas: Observations from the Caribbean and Great Barrier Reef regions. *Cont. Shelf Res.* **2014**, *82*, 85–98. [[CrossRef](#)]
53. Weihs, R.R.; Bourassa, M.A. Modeled diurnally varying sea surface temperatures and their influence on surface heat fluxes. *J. Geophys. Res. Oceans* **2014**, *119*, 4101–4123. [[CrossRef](#)]
54. Martin, M.; Dash, P.; Ignatov, A.; Banzon, V.; Beggs, H.; Brasnett, B.; Cayula, J.-F.; Cummings, J.; Donlon, C.; Gentemann, C.; et al. Group for High Resolution Sea Surface temperature (GHRSSST) analysis fields inter-comparisons. Part 1: A GHRSSST multi-product ensemble (GMPE). *Deep Sea Res. Part II* **2012**, *77–80*, 21–30. [[CrossRef](#)]
55. Marullo, S.; Santoleri, R.; Ciani, D.; Borgne, P.L.; Péré, S.; Pinardi, N.; Tonani, M.; Nardone, G. Combining model and geostationary satellite data to reconstruct hourly SST field over the Mediterranean Sea. *Remote Sens. Environ.* **2014**, *146*, 11–23. [[CrossRef](#)]